Electron paramagnetic resonance of *n*-type semiconductors for applications in three-dimensional thermometry

Darshan Chalise [1,2,*] and David G. Cahill [1,2,3]

[1] *Department of Physics, University of Illinois at Urbana-Champaign, Urbana, Illinois, 61801, USA*
[2] *Materials Research Laboratory, University of Illinois at Urbana-Champaign, Urbana, Illinois, 61801, USA*
[3] *Materials Science and Engineering, University of Illinois at Urbana-Champaign, Urbana, Illinois, 61801, USA*

(Received 15 September 2023; accepted 20 November 2023; published 13 December 2023)

While there are several two-dimensional thermometry techniques that provide excellent spatial, temporal, and time resolution, there is a lack of three-dimensional (3D) thermometry techniques that work for a wide range of materials and offer good resolution in time, space, and temperature. We investigate electron paramagnetic resonance (EPR) of *n*-type silicon and germanium as a possible means of 3D thermometry. While in germanium the EPR linewidths are too broad for thermometry, EPR linewidths in silicon are reasonably narrow and exhibit a strong temperature dependence. The temperature dependence of the spin-lattice relaxation rate ($1/T_1$) of conduction electrons in *n*-type Si have been extensively studied for low dopant concentrations and follows a T^3 law due to phonon broadening. For heavily doped Si, which is desirable for good SNR for application in thermometry, impurity scattering is expected to decrease the temperature dependence of $1/T_1$. Our results show that, in heavily doped *n*-type Si, spin-lattice relaxation induced by impurity scattering does not drastically decrease the temperature dependence of EPR linewidths. In P-doped Si with donor concentration of $7 \times 10^{18}/\mathrm{cm}^3$, the EPR linewidth has a $T^{5/2}$ temperature dependence; the temperature dependence decreases to $T^{3/2}$ when the donor concentration is $7 \times 10^{19}/\mathrm{cm}^3$. While the temperature dependence of linewidth decreases for heavier doping, EPR linewidth is still a sensitive thermometer. We define a figure of merit for SNR for thermometry from EPR linewidths of *n*-type Si and observe that increasing the doping results in a better SNR for thermometry. Using effective medium theory, we show that EPR linewidth can be a sensitive thermometer for application in 3D thermometry with systems embedding microparticles of heavily doped *n*-type Si.

DOI: 10.1103/PhysRevApplied.20.064024

I. INTRODUCTION

While sensitive and spatially well resolved invasive [1] and noninvasive [2] two-dimensional (2D) thermometry techniques have been established, there is a general lack noninvasive three-dimensional (3D) thermometry techniques. This is especially true in systems where there is no optical access. 3D thermometry in optically opaque systems is, however, useful in biology [3] and engineering [4].

Imaging of systems opaque to visible light can be performed using electromagnetic waves of much higher (x ray) or lower frequencies (radio frequencies or microwave frequencies) [5]. 3D x-ray imaging is possible in both absorption [6] and diffraction mode [7]. However, x-ray absorption is not strongly temperature dependent and x-ray diffraction requires crystalline materials [4]. Even for crystalline materials, XRD requires sufficiently high-energy x rays for 3D thermometry [4].

Different NMR processes depend on temperature [3], and therefore, nuclear magnetic resonance imaging, i.e., (N)MRI, can be used to obtain spatially resolved 3D temperature maps. In biological systems, (N)MRI has been used to obtain temperature maps using spin-density contrast [8], spin-lattice relaxation time (T_1) contrast [9], spin-spin relaxation time (T_2) contrast [10,11], chemical shift contrast [12,13], and diffusion contrast [11,14]. While spin density and the relaxation-time contrasts are relatively less sensitive to temperature, diffusion and chemical shift contrast suffer from motional artifacts [3]. Additionally, all these techniques depend on the nature of water for the temperature dependence of the NMR signal [3], and therefore, cannot be applied in systems not containing water.

In our previous work, we showed temperature-dependent diffusion results in temperature-dependent motional narrowing of NMR lines in the presence of superparamagnetic iron-oxide nanoparticles (SPIONs). The subsequent spin-spin relaxation time (T_2) is a thermometer in fluids in the presence of SPIONs [15]. The method,

*darshan2@illinois.edu

 © 2023 American Physical Society

however, is restricted to fluids where the timescale of diffusion is fast enough to even out the field inhomogeneities induced by the SPIONs. The field inhomogeneities induced by the SPIONs (the magnetization of the SPIONs) is not strongly temperature dependent. The method is, therefore, limited to fluids where the temperature dependence of diffusion is strong.

In general, NMR is limited to systems where the nucleus of interest has a fast enough diffusion to give an observable NMR spectrum. This makes NMR thermometry not applicable in most solids.

3D imaging using magnetic resonance, however, is not limited to nuclear spin resonances. Electron paramagnetic resonance (EPR) could also be used for 3D imaging of systems with paramagnetic electrons or free radicals [16]. Temperature-dependent EPR signal has also been suggested for possible thermometry [17]. Therefore, EPR imaging (EPRI) provides an opportunity for 3D thermometry in systems where x ray or NMR cannot obtain the temperature information.

In a paper reporting EPR in semiconductors, Kittel and Brattain [18] noted that the EPR linewidth of conduction electrons in n-type silicon is highly sensitive to temperature at elevated temperatures (>100 K). This was further confirmed by works by Lancaster [19] and Lepine [20]. Theories by Elliot [21] and Yafet [22] and further improved by others [23–25] showed that phonon broadening results in an approximately T^3 temperature dependence of EPR linewidth in n-type Si. In p-type silicon, however, the broadening of resonance of the acceptor states by internal stresses from dislocations is much more significant than the broadening of resonance of the donor states in n-type silicon [26], and resonance in p-type Si is not observed until the sample is subjected to a uniaxial stress [27]. Thus, thermometry using EPR linewidth in p-type Si might not be possible. EPR linewidth in n-type Si, on the other hand, can be a sensitive 3D thermometer.

For heavily doped Si, which is preferred for a higher SNR in thermometry, impurity scattering is expected to impact the line broadening of EPR spectrum [28–30]. There is a need for a systematic study on how the impurity impacts the temperature dependence of EPR linewidths at higher temperatures. In this paper, we investigate the temperature dependence of EPR linewidth of n-type Si at different carrier densities to identify the optimal doping level for application in thermometry. We also study the EPR linewidths in n-type Ge to investigate if Ge provides a better opportunity for 3D thermometry. This work reports the temperature dependence of EPR linewidth of highly doped n-type silicon at high temperatures. Therefore, the work is of potential interest to both thermometry and spintronics communities.

Finally, we apply effective medium theory to estimate the penetration depths of microwave at different doping levels and frequencies.

TABLE I. Resistivities and carrier densities for studied samples.

Sample no.	Type	Resistivity (mΩ cm)	Carrier concentration, n_c (cm^{-3})
A	P-doped Si	1.01	7×10^{19} [31]
B	P-doped Si	8.3	7×10^{18} [32]
C	P-doped Si	105	7×10^{16} [31]
D	P-doped Si	4300	9×10^{14} [31]
E	P-doped Si	528 000	7×10^{12} [32]
F	As-doped Ge	25	5×10^{17} [33]
G	Sb-doped Ge	7.9	1.5×10^{18} [33]

The study of the sensitivity of the temperature dependence along with the estimation of the penetration depth required for volumetric imaging using electron paramagnetic resonance imaging (EPRI) provide an understanding of the potential of EPRI for 3D thermometry.

II. EXPERIMENTAL DETAILS

P-doped Si with different carrier concentrations were purchased from Sil'Tronix Silicon Technologies and As-doped and Sb-doped Ge were purchased from El-Cat Inc. The room-temperature sheet resistance and resistivity of the wafers was measured by using a four-point probe using a constant current source and Keithly 2000 as a dc voltmeter. Table I summarizes the measured room-temperature resistivities and corresponding carrier concentrations for each sample.

Temperature-controlled EPR measurements from 100 to 290 K were carried out on a Bruker EMXPlus spectrometer operating at a frequency of approximately 9.4 GHz (X band). The magnetic field was swept with a modulation frequency of 100 kHz. For measurements on Si, the modulation amplitude for most measurements were set at 1 G but was reduced if the EPR linewidths were comparable to or smaller than 1 G. For Ge, the EPR lines were very broad (approximately 40 G) for all temperatures, and therefore, a modulation amplitude of 10 G was used to maximize the signal to noise ratio. To confirm the line broadening was independent of the field used, additional measurements were also performed on an ELEXSYS E500 (E580) spectrometer operating at microwave frequencies of 34 GHz (Q band) and 3.5 GHz (S band).

Samples not ground to powders showed a Dysonian lineshape [34,35] at the expected g values of conduction electrons. This is expected for highly conductive samples where microwave penetration depths are smaller than the particle size [36]. The effect was more pronounced at 34 GHz as the penetration depth is reduced further. Therefore, the samples were ball milled using alumina balls and a jar and inspected with scanning electron microscopy to ensure the average particle sizes were smaller than the

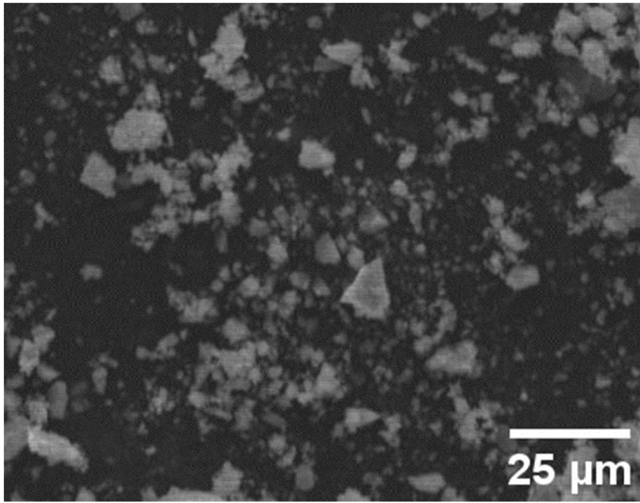

FIG. 1. SEM image of P-doped Si ($n_c = 7 \times 10^{19}$ cm^{-3}) after ball milling. The image was taken in a FEI Quanta FEG 450 SEM with an incident electron energy of 20 keV. The volume average particle size, determined from ImageJ, is approximately 8 μm. The standard deviation is approximately 13 μm.

microwave penetration depth (approximately 10 μm for Si with $n_c = 7 \times 10^{19}$ cm^{-3} at 9.3 GHz). The Dysonian effect was removed, and the line shape could be fit well with Lorentzian lineshape using EasySpin tool in MATLAB. The SEM image after ball milling is presented in Fig. 1. The average particle size after the ball milling was approximately 8 μm with a standard deviation of approximately 13 μm. An example fit of the spectra with Lorentzian lineshape is presented in Appendix A.

Ball milling, however, resulted in an additional feature in the EPR spectrum, which has been attributed in n-type semiconductor to a paramagnetic state created due to dangling bonds formed by ball-milling damage [37,38]. In silicon, it had been suggested that heating the sample in air at 800 °C anneal the damage to remove the feature [38]. We were able to remove this feature when the powdered samples were heated in a muffle furnace at 800 °C.

The comparison of lineshapes before ball milling, after the ball milling, and after heating the ball-milled sample at 800 °C are included in Fig. 2.

Surface states will pin the Fermi energy midgap at the surface of the particles and create a depletion region near the surface. The maximum width of the depletion region is given by $L_{\text{depletion}} = \sqrt{(4\varepsilon k_B T \ln(n_c/n_{\text{Si}}))/e^2 n_c}$ [39]. Here, $\varepsilon = 11.9\ \varepsilon_0$ is the dielectric constant of pure Si, $n_{\text{Si}} = 1.45 \times 10^{10}$ cm^{-3} is the concentration of free carriers in pure Si, k_B is the Boltzmann constant, and e is the charge in an electron. The maximum widths of the depletion region in the sample with $n_c = 7 \times 10^{19}$ cm^{-3}, $n_c = 7 \times 10^{18}$ cm^{-3}, and $n_c = 7 \times 10^{16}$ cm^{-3} are 5, 13, and 120 nm, respectively. In samples with particle size comparable to the depletion length, the shape of the conduction band can change significantly due to the presence of the surface states. In our samples, however, the particle size is approximately 8 μm. Therefore, we do not expect the density of conduction electrons to be strongly influenced by surface states.

III. RESULTS

We were able to observe EPR of conduction electrons ($g \approx 1.998$ [40]) in P-doped Si with carrier densities $n_c = 7 \times 10^{19}$ cm^{-3}, $n_c = 7 \times 10^{18}$ cm^{-3}, and $n_c = 7 \times 10^{16}$ cm^{-3} in the entire temperature range of our investigation, i.e., 100–290 K. We also observed EPR of conduction electrons ($g \approx 1.57$ [41,42]) in As-doped Ge ($n_c = 5 \times 10^{17}$ cm^{-3}) from 50 to 170 K. Above 170 K, the EPR linewidth was too broad for the spectra to be observable.

For P-doped Si with $n_c = 7 \times 10^{12}$ cm^{-3}, we did not observe any EPR signal for expected values of conduction electrons ($g = 1.998$ [40]). Even for the Si with $n_c = 9 \times 10^{14}$ cm^{-3}, the EPR signal was too weak to make conclusions on the dependence of the linewidth and integrated intensities on temperature. We also did not observe EPR in conduction electrons in Sb-doped Ge. The lack of observation in EPR in Sb-doped Ge has been attributed to strain broadening of the spectra, which causes resonance to be too broad to be observed during the EPR experiment [43].

For conduction electrons in n-type semiconductors, the spin-spin relaxation ($1/T_2$) is suppressed due to motional narrowing of the conduction electrons, and the observed linewidth of the EPR spectra is limited by spin-lattice relaxation ($1/T_1$) [19,21].

The temperature dependence of the spin-lattice relaxation rate of conduction electrons in semiconductors was studied by Elliot predicting the spin-flip probabilities due to momentum scattering of the electrons with the lattice [21]. Yaffet also included the contribution of the modulation of spin-orbit coupling due to lattice vibration [22]. Elliot-Yaffet theory predicts a $T^{5/2}$ temperature dependence of the of the spin-lattice relaxation rate due to electron-phonon scattering for intravalley scattering of electrons by phonons [22,23]. The formalisms by Cheng *et al.* [23] and Park *et al.* [25] pointed out that at higher temperature intervalley scattering of electrons by phonons dominates the spin-lattice relaxation and the spin-lattice relaxation rate follows a T^3 power law.

Figure 3(a) shows the temperature dependence of EPR linewidths of P-doped Si samples with $n_c = 7 \times 10^{16}$/cm^3, $n_c = 7 \times 10^{18}$/cm^3, and $n_c = 7 \times 10^{19}$/cm^3 as well as As-doped Ge with $n_c = 5 \times 10^{17}$/cm^3. For P-doped Si with $n_c = 7 \times 10^{19}$/cm^3, we also performed the comparison of linewidths between silicon powder in air to silicon powder

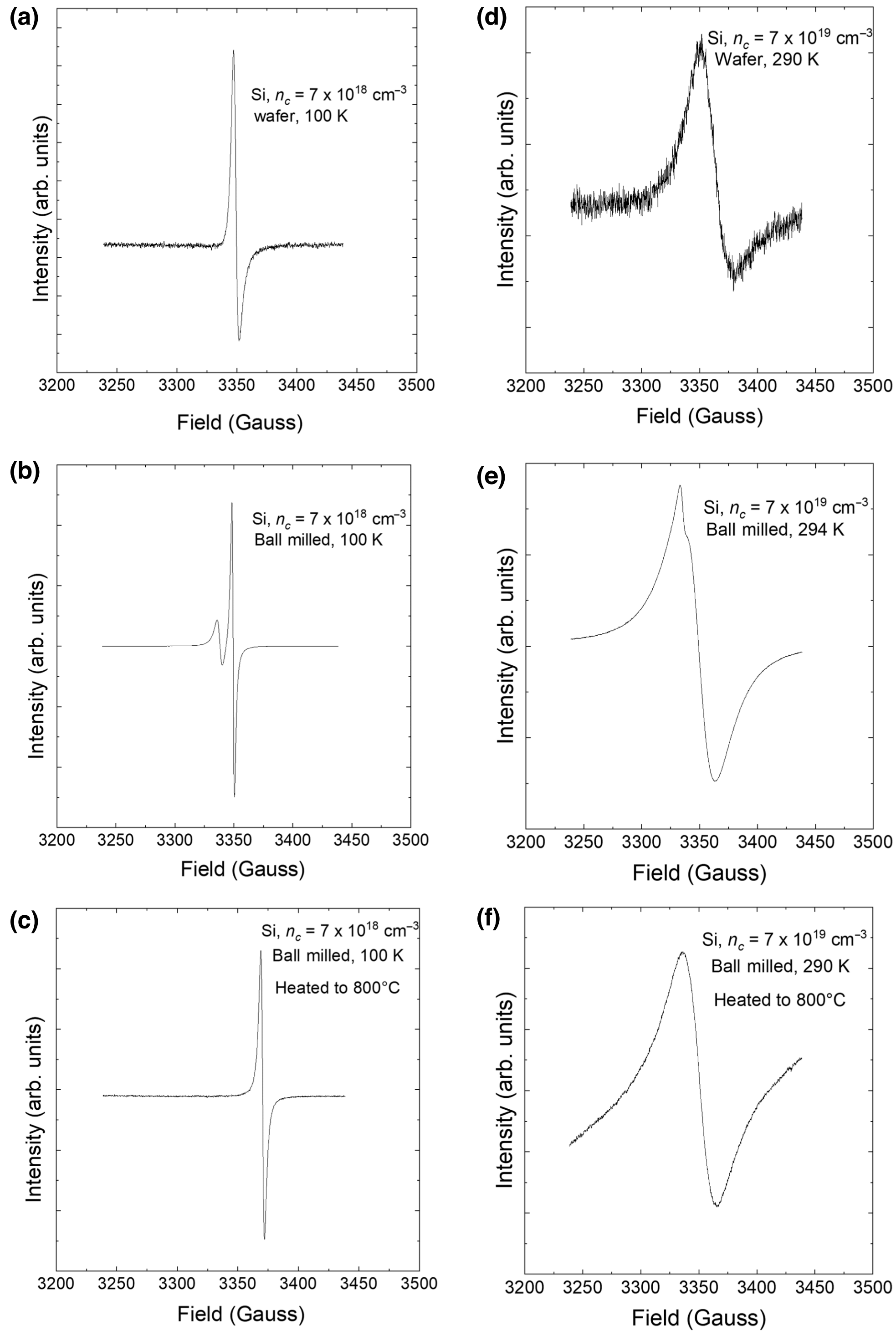

FIG. 2. Comparison of EPR spectra in P-doped Si ($n_c = 7 \times 10^{18}$ cm^{-3}) at 100 K (a)–(c) and P-doped Si ($n_c = 7 \times 10^{19}$ cm^{-3}) at 290 K. (a) Before the sample is ball milled, (b) after ball milling but before heating at 800 °C, and (c) after ball milling and heating at 800 °C. The recorded spectra is a derivative spectra with a central field sweep of 200 G at a modulation amplitude of 1 G and a modulation frequency of 100 kHz. The peak-to-peak linewidth ($\Delta B_{\text{p-p}}$) is $1/\sqrt{3}$ times the full-width at half-maximum of the absorption spectra. The spectra were baseline corrected for analysis in EasySpin. (a),(d) show a Dysonian lineshape as the particle size (300-μm-thick wafer) is larger than the microwave penetration depth (approximately 20 μm for $n_c = 7 \times 10^{18}$ cm^{-3} and approximately 10 μm for $n_c = 7 \times 10^{19}$ cm^{-3} at 9.4 GHz). (b),(e) show the Dysonian effect is removed after ball milling but ball-milling results in paramagnetic surface states that appear in the EPR spectra. (c),(f) show that annealing the sample at 800 °C removes the paramagnetic surface states.

embedded in epoxy. Embedding in epoxy did not change the linewidth of the resonance or the temperature dependence of integrated intensities. The comparison of the samples simply in powder form and embedded in epoxy is included in Appendix C. The linewidths in Ge above 170 K are too broad, and the SNR is too low to make any conclusions about the temperature dependence.

The linewidths in Si are compared with experimental data from Lancaster [19] and Lepine [20] as well as the theory by Cheng *et al*. [23]. Our data for the sample with $n_c = 7 \times 10^{16}/\mathrm{cm}^3$ as well as the data from Lancaster and Lepine for similarly doped samples show that the predictions of the EPR linewidth from Cheng *et al*. matches reasonably well for low-doped samples and follows an approximately T^3 trend.

For heavily doped samples, the EPR linewidths are much broader than the phonon-broadened linewidth predicted by Cheng. For heavily doped samples, impurity scattering is expected to affect the spin-lattice relaxation rate [28–30]. Figure 3(b) includes results from subtracting the phonon-broadened linewidth. This remnant linewidth, which can be attributed to impurity scattering follows a temperature dependence that is only slightly smaller than $T^{3/2}$. This is in contrast to the formalism by Song *et al*. [30] where the temperature dependence of impurity scattering for heavily doped samples is expected to be $\sqrt{T}$. Therefore, results on heavily doped *n*-type Si show that the theory predicting the effect of impurity scattering on spin relaxation requires a revision.

For application in thermometry, the high-temperature dependence of impurity scattering induced spin-lattice relaxation means that EPR linewidth is a highly sensitive thermometer for high-doped silicon.

It is useful to define a sensitivity coefficient, ξ_S^T, which defines the percentage change in signal S for 1% change in the absolute temperature T, $\xi_S^T = d \ln p / d \ln T$ [44]. For Si with high density of carriers, the temperature dependence of EPR linewidth is close to T^3 and $\xi_{\Delta\nu}^T \approx 1.5$.

For higher carrier densities, i.e., $n_c \approx 7 \times 10^{18}/\mathrm{cm}^3$ and $n_c \approx 7 \times 10^{19}/\mathrm{cm}^3$, the temperature dependence decreases to approximately $T^{5/2}$ and approximately $T^{3/2}$. Therefore, the respective sensitivities to temperature decrease to approximately 2.5 and approximately 1.5.

We also investigated whether the integrated intensity of the EPR spectrum can be used for sensitive thermometry (using the spin-density contrast). In the nonmetallic Si, the magnetic susceptibility of conduction electrons follows the Curie-Weiss law [45]. Therefore, we expect the temperature dependence of the integrated intensity to follow a T^{-1} dependence. Figure 4 shows this is in fact the case in our measurements where at high temperatures, the integrated intensity of the EPR spectra in Si with $n_c = 7 \times 10^{16}$ cm^{-3} follows a T^{-1}. The sensitivity of the integrated intensity to temperature in these samples is, therefore, -1, which is smaller compared to the temperature dependence of the

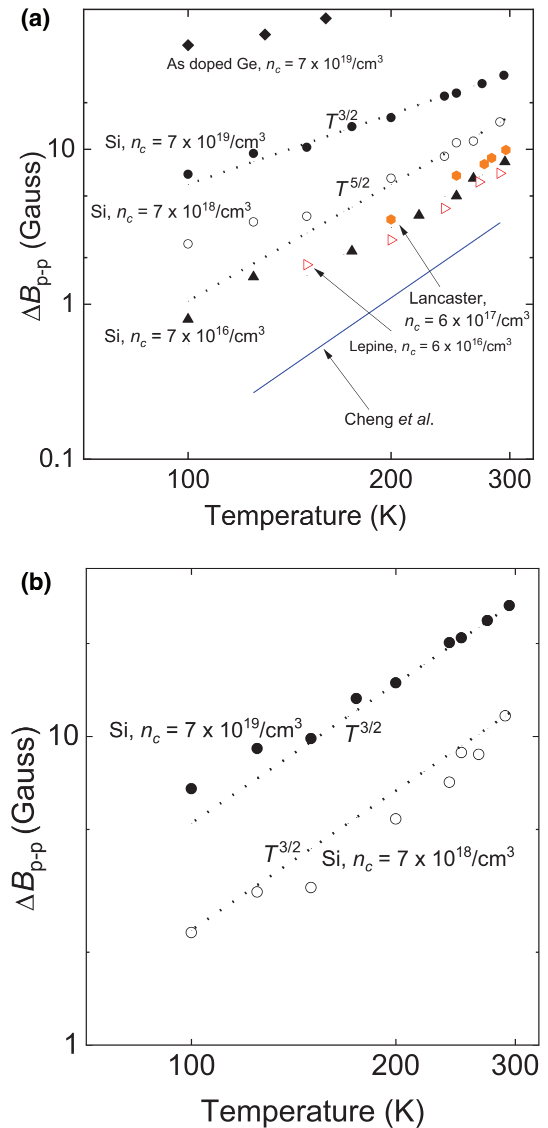

FIG. 3. Temperature dependence of peak-to-peak EPR linewidth, $\Delta\nu_{\text{p-p}}$. (a) Shows the experimental linewidths of P-doped Si with carrier densities $n_c = 7 \times 10^{19}$ cm^{-3} (filled black circles), $n_c = 7 \times 10^{18}$ cm^{-3} (open black circles), $n_c = 7 \times 10^{16}$ cm^{-3} (filled black triangles) and As-doped Ge with $n_c = 5 \times 10^{17}$ cm^{-3} (filled black diamonds). Experimental data by Lepine [20] (open red forward triangles) and Lancaster [19] (filled orange hexagon) and the theoretical linewidth predicted by Cheng *et al*. [23] (blue solid line) are included for comparison. $\Delta\nu_{\text{p-p}}$ of Si with $n_c = 7 \times 10^{19}$ cm^{-3} and $n_c = 7 \times 10^{18}$ cm^{-3} shows an approximately $T^{3/2}$ and approximately $T^{5/2}$, respectively, near room temperature. (b) shows the residual linewidth of Si with $n_c = 7 \times 10^{19}$ cm^{-3} (filled black circles) and $n_c = 7 \times 10^{18}$ cm^{-3} (open black circles) after subtracting the phonon-broadened contribution predicted by Cheng *et al*. [23]. The residual linewidths show a temperature dependence slightly smaller than $T^{3/2}$. The data at 125, 175, and 250 K for samples with $n_c = 7 \times 10^{19}$ cm^{-3} and $n_c = 7 \times 10^{18}$ cm^{-3} and at 250 K for the sample with $n_c = 7 \times 10^{16}$ cm^{-3} are taken with sample weight approximately 1 mg. All other measurements are taken with sample weight approximately 4 mg.

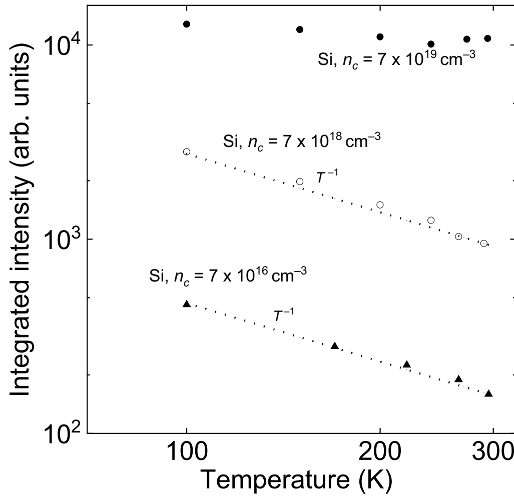

FIG. 4. Temperature dependence of integrated EPR intensities for P-doped Si samples with carrier concentration $n_c = 7 \times 10^{19}$ cm^{-3} (filled circles), $n_c = 7 \times 10^{18}$ cm^{-3} (open circles), and $n_c = 7 \times 10^{16}$ cm^{-3} (filled triangles). The presented data for each sample is normalized with Q value of the resonance cavity at each temperature. The data for As-doped Ge is not included as the EPR intensity was too low to run EasySpin simulation and estimate the integrated intensity. P-doped Si samples with carrier densities $n_c = 7 \times 10^{18}$ cm^{-3} and $n_c = 7 \times 10^{16}$ cm^{-3} show a T^{-1} dependence of the integrated intensity while the sample with $n_c = 7 \times 10^{19}$ cm^{-3} does not show a significant temperature dependence.

linewidth. Even for the Si with $n_c = 7 \times 10^{18}$ cm^{-3}, the integrated intensity follows a T^{-1} relationship.

In degenerately doped Si, we expect Pauli paramagnetism, where the susceptibility is independent of temperature. Our measurement on the silicon sample with $n_c = 7 \times 10^{19}$ cm^{-3}, shows no temperature dependence of the integrated intensity.

The difference of the temperature dependence of integrated intensity of extremely metallic and nonmetallic Si also enables spin-density contrast to decouple the contribution from concentration and temperature in systems with different doping levels.

Finally, we also investigated the temperature dependence of the linewidth and the integrated intensity of the states formed by ball milling on different silicon and germanium samples. For all Si samples, these surface states gave a resonance at $g \approx 2.005$ [37]. For Ge samples, the resonance of the surface state was at $g \approx 2.004$ [37]. The integrated intensity of the surface states increased with the extent of milling and decreased with doping—we observed that small pieces of uncrushed wafers did not give any surface-state resonance, while low-doped Si showed resonance of surface states after crushing in mortar and pestle and heavily doped Si ($n_c = 7 \times 10^{18}$ cm^{-3} and $n_c = 7 \times 10^{19}$ cm^{-3}) showed a surface-state resonance only

TABLE II. Figure of merit, f, for EPR thermometry for silicon with $n_c = 7 \times 10^{16}$ cm^{-3}, 7×10^{18} cm^{-3}, and 7×10^{19} cm^{-3}. Carrier densities are normalized to $n_c = 7 \times 10^{16}$ cm^{-3} in the table.

Sample	Normalized carrier density (n_c)	Peak-peak linewidth ($\Delta\nu$) at 290 K (Gauss)	Sensitivity of linewidth to temperature: $S_T^{\Delta\nu} = d\ln\Delta\nu / d\ln T$	$S_T^{\Delta\nu} n_c/\Delta\nu$
C	1	8	3	0.38
B	100	15	2.5	16.67
A	1000	30	1.5	50

after ball milling. The surface states did not show any significant change in linewidth as a function of temperature while the integrated intensity followed an approximately T^{-1} trend. The results of the linewidth and intensity measurements of surface states are included in Appendix B.

Since the surface states do not offer any advantage in terms of thermometry, removing the surface states so that it does not affect the EPR image yields the best results for thermometry using semiconductors.

IV. DISCUSSION AND CONCLUSIONS

We have systematically investigated the temperature dependence of linewidth and intensities of EPR of conduction electrons in Si at different doping levels and compared it to EPR of conduction electron in Ge. Our results show that while EPR in Ge and lightly doped Si ($n_c \leq 1 \times 10^{16}$/cm^3) are not appropriate for thermometry near room temperature, heavily doped Si shows a strong temperature dependence of linewidth, which could be used for 3D thermometry.

Since higher carrier densities and higher-temperature sensitivity results in an increased SNR while broader linewidths mean reduced resonance lifetimes, we can define a figure of merit, f, for thermometry as the product of the carrier density n_c and temperature sensitivity $S_T^{\Delta\nu}$ divided by the EPR linewidth $\Delta\nu$. Table II shows the figure of merit for Si with $n_c = 7 \times 10^{19}$ cm^{-3}, 7×10^{18} cm^{-3}, and 7×10^{16} cm^{-3}. It can be seen from Table II that increasing doping results in a better thermometer. Therefore, for thermometry applications where Si is embedded in a matrix, n-type Si with highest possible doping is optimal.

A general problem for EPR imaging on heavily doped semiconductors is the reduced microwave penetration depth due to conductivity of the sample. Even for a microwave of frequency 1 GHz, the penetration depth for Si with resistivity 1 mΩ cm is only approximately 50 μm

[19]. For imaging of devices with thick Si (e.g., 3D integrated circuits), application of EPR for 3D thermometry is challenging.

To evaluate the possibility of embedding Si as a contrast agent in dielectric samples, we use effective medium theory to calculate the microwave penetration depth in the Si-dielectric composite. We have applied Bruggeman's effective medium theory [46] to evaluate the dielectric response of a medium with water (resembling most tissues) and low-volume fractions of Si at microwave frequencies of 1 and 10 GHz.

The details of the effective-medium theory and the values of the optical constants of Si and water are included in Appendix D. The simulation is performed for infinitesimal particles of silicon homogenously distributed in pure water. We use water as a reference to resemble the potential application in biological tissues, which mostly contain water. If the water contains ionic impurities, both the frequency-dependent and the static parts of the dielectric constant of the water will be modified. We point the readers to the work by Hasted [47] for a description of the effect of ionic impurities on the dielectric constant of water and the work by Nortemann *et al*. [48] when the ionic impurity is sodium chloride.

Figure 5 shows the microwave penetration depth of water-Si composite at 298 K for volume fraction of Si between 0–0.1 the volume of water at 1 and 10 GHz for Si with carrier concentrations $n_c = 7 \times 10^{19}$ cm^{-3}, 7×10^{18} cm^{-3}, and 7×10^{16} cm^{-3}. Effective-medium theory shows that, for very low volume fractions of Si in a host material, the microwave penetration depth is primarily determined by the microwave properties of the host material.

At 10 GHz (at 298 K), the penetration depth of microwave in water is less approximately 1 mm. Therefore, application of 3D thermometry in water using EPR is challenging. At 1 GHz, however, the penetration depth is approximately 10 cm, and 3D EPR imaging of systems with large volumes is possible. At 298 K, the imaginary part of the dielectric function peaks near 10 GHz, and therefore the penetration depth, is significantly reduced. We point the readers to the work by Andryieuski *et al*. [49] for estimating the dielectric function of pure water at different frequencies. At frequencies where the dielectric loss is not significant, our results show, embedding low-volume fraction of heavily doped Si in biological fluids can provide a means of sensitive 3D thermometry.

Imaging at low microwave frequency and low-volume fractions, however, results in reduced signal-to-noise ratio. Future studies should include the quantification of the signal-to-noise ratio when small voxel sizes are imaged and lower frequencies are applied.

ACKNOWLEDGMENTS

The authors are grateful to Dr Toby Woods of the School of Chemical Sciences, University of Illinois at Urbana Champaign for assistance with the EPR measurements.

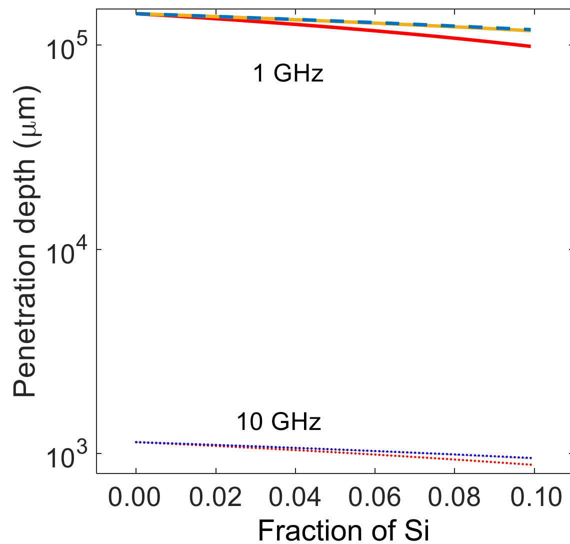

FIG. 5. Calculated microwave penetration depth in a water–Si composite at 1 GHz (dotted lines) and 10 GHZ (red and orange solid lines and blue dashed line). The results are calculated using Bruggeman's symmetric effective medium theory for Si volume fractions from 0 to 0.1 times the volume of water and for Si carrier densities $n_c = 7 \times 10^{19}$ cm^{-3} (blue), 7×10^{18} cm^{-3} (orange), and 7×10^{16} cm^{-3} (red).

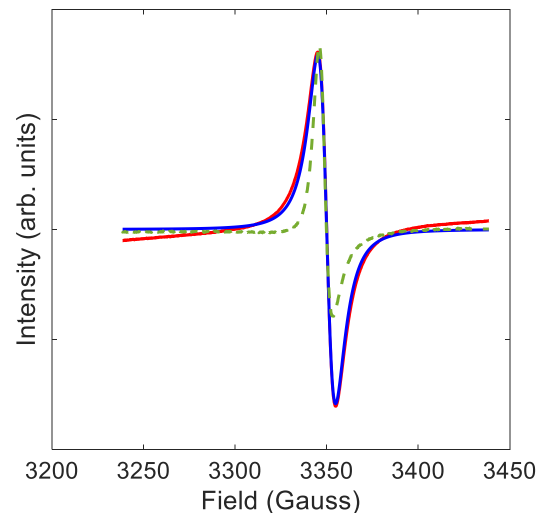

FIG. 6. Lorentzian fit (blue line) to experimental EPR data (red line) for P-doped Si with ($n_c = 7 \times 10^{19}$ cm^{-3}) after ball milling and annealing at 800 °C. The fit is performed for the data at 125 K using EasySpin toolbox in MATLAB with a Lorentzian function. For comparison, the spectra of uncrushed wafer is also included (green dashed line). The intensity of the uncrused wafter is increased by a factor of 3 for comparison with the ball-milled sample. The uncrushed wafer showed a Dysonian lineshape and was not appropriate to fit with a Lorentzian function.

This project was funded by Semiconductor Research Corporation (Task ID: 3044.001). Major funding for Bruker EMXPlus was provided by National Science Foundation Award 1726244 (2017) to the School of Chemical Sciences EPR Lab at the University of Illinois.

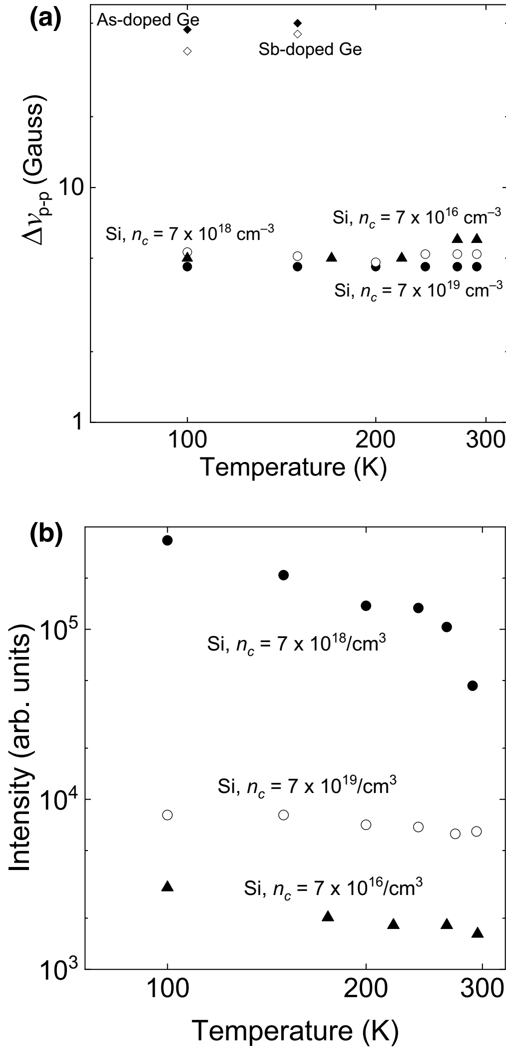

FIG. 7. Temperature dependence of (a) EPR linewidths and (b) integrated intensities of the surface states formed after ball milling. Results included are for Si with $n_c = 7 \times 10^{19}$ cm^{-3} (filled circles), $n_c = 7 \times 10^{18}$ cm^{-3} (open circles), and $n_c = 7 \times 10^{16}$ cm^{-3} (filled triangles), As-doped Ge with $n_c = 5 \times 10^{17}$ cm^{-3} (filled diamonds) and Sb doped Ge with $n_c = 1.5 \times 10^{18}$ cm^{-3} (open diamonds). EPR from surface states in P-doped Si were observable for the entire range of acquisition (100 K–290 K) and did not show much temperature dependence of linewidths. Surface states in both Sn-doped and As-doped Ge were broad and linewidth measurements could not be performed over 170 K. The intensities in Ge is not presented as the signal-to-noise ratio was too small for meaningful comparison.

APPENDIX A: EXAMPLE FIT OF EPR SPECTRA IN BALL-MILLED SILICON WITH LORENTZIAN LINESHAPE USING EasySpin

An example of Lorentzian fit to the EPR data using EasySpin is shown in Fig. 6 for P-doped Si with $n_c = 7 \times 10^{19}$/cm^3 at 125 K after the sample is ball-milled and annealed at 800 °C. For comparison, the Dysonian lineshape displayed by the uncrushed wafer at 125 K is also shown.

APPENDIX B: EPR LINEWIDTHS AND INTENSITIES OF THE SURFACE STATES

The temperature dependence of the EPR linewidth of the surface states formed after ball-milling is shown in Fig. 7(a). The temperature dependence of the integrated

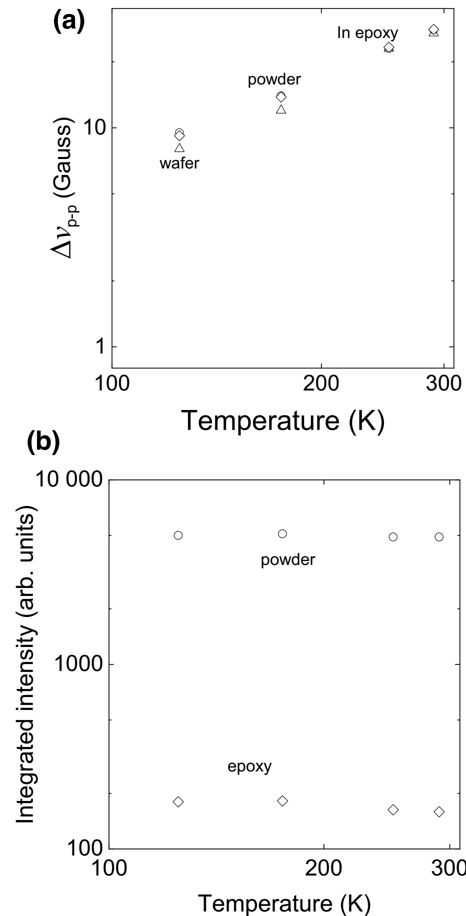

FIG. 8. Comparison of (a) EPR linewidth and (b) integrated intensities in P-doped Si with $n_c = 7 \times 10^{19}$ cm^{-3} in ball-milled Si powder (open circles), ball-milled Si embedded in epoxy (open diamonds) and 2 cm × 3 mm × 300 μm, uncrushed Si wafer (open triangle). The integrated intensity in Si wafer is not presented as a Lorentzian fit could not be performed on the Dysonian lines. The mass of Si in powder form is approximately 1 mg while the mass of Si embedded in epoxy is approximately 0.1 mg.

TABLE III. Dielectric constants of investigated Si samples at 1 and 10 GHz.

Sample	Carrier concentration, n_c (cm^{-3})	Average collision time, τ(s)	Plasma frequency, ω_p (Hz)	ε (1 GHz)	ε (10 GHz)
A	7×10^{19}	7.6×10^{-15}	8.3×10^{14}	$-38 + \mathrm{i}\,(1.0 \times 10^{6})$	$-38 + \mathrm{i}\,(1.0 \times 10^{5})$
B	7×10^{18}	1.6×10^{-14}	2.9×10^{14}	$-11 + \mathrm{i}\,(2.2 \times 10^{5})$	$-11 + \mathrm{i}\,(2.2 \times 10^{4})$
C	7×10^{16}	1.2×10^{-13}	2.9×10^{13}	$-0.57 + \mathrm{i}\,(1.6 \times 10^{4})$	$-0.57 + \mathrm{i}\,(1.6 \times 10^{3})$

intensities of the surface states in P-doped Si is shown in Fig. 7(b).

APPENDIX C: COMPARISION OF EPR LINEWIDTHS AND INTENSITIES IN Si WAFER AND BALL-MILLED *n*-TYPE Si IN POWDER FORM AND EMBEDDED IN EPOXY

The comparison of EPR linewidths in Si wafers, ball-milled Si in powder form and ball-milled Si embedded in epoxy are included in Fig. 8(a). The temperature dependence of integrated intensities in ball-milled powder and the ball-milled Si embedded in epoxy are included in Fig. 8(b).

APPENDIX D: EFFECTIVE-MEDIUM THEORY CALCULATIONS FOR SILICON-WATER COMPOSITE

We use the Drude model to estimate the dielectric constants of Si at different carrier concentrations and different frequencies. For the carrier concentrations used in our experiment, the dielectric properties predicted by the Drude model match well with experimental observation [50]. In SI units, the relative dielectric constant is given by [51]

$$\varepsilon(\omega) = \varepsilon_\infty + \frac{\omega_p^2}{\omega(\omega + i\Gamma)}.$$

Here, ω is the probing frequency and $\varepsilon_\infty = 11.7$ [52] is the contribution due to bound electrons. $\omega_p = \sqrt{n_c e^2/\varepsilon_0 m}$ is the plasma frequency for a material with carrier density n_c and effective mass of the carrier m. e is the charge of an electron and ε_0 is the permittivity of free space. $\Gamma = 1/\tau$ is the electron damping rate for an average collision time τ.

The real and imaginary components of the relative dielectric constant are given by

$$\varepsilon_{\mathrm{real}}(\omega) = \varepsilon_\infty + \frac{\omega_p^2}{(\omega^2 + \Gamma^2)},$$

$$\varepsilon_{\mathrm{imaginary}}(\omega) = \frac{\omega_p^2}{\omega\Gamma(1 + (\omega/\Gamma))}.$$

For Si with $n_c = 7 \times 10^{19}$ cm^{-3}, τ is taken from data by Slaoui *et al.* [53]. For Si with $n_c = 7 \times 10^{18}$ cm^{-3} and $n_c = 7 \times 10^{16}$ cm^{-3}, τ is calculated from the mobility (μ) data [54] using $\mu = e\tau/m$ [51] with $m \approx 0.26\, m_e$ [55], $m_e = 9.1 \times 10^{-31}$ kg. For $n_c = 7 \times 10^{19}$ cm^{-3}, $m \approx 0.29\, m_e$ [55] has been used to calculate the plasma frequency.

Table III summarizes the relative dielectric constant for Si at different frequencies and carrier concentration. As it can be seen from the table, the real part of the dielectric constant is predominantly determined by the collision frequency at the frequency limit of our measurements. Therefore, there is no significant change in the real part of the dielectric constants at $\omega = 2\pi \times 1$ GHz and $\omega = 2\pi \times 10$ GHz. The imaginary part scales with $1/\omega$.

The dielectric constants of water are $\varepsilon = 80 + 3\mathrm{i}$ at 1 GHz and $65 + 35\mathrm{i}$ at 10 GHz [49].

For a Si-water composite with the complex dielectric constants of Si and water $\varepsilon_{\mathrm{Si}}$ and ε_w, respectively, the dielectric constant, ε, of the composite with Si volume fraction f is calculated using Bruggeman's mixing formula [56]:

$$\frac{\varepsilon - \varepsilon_w}{\varepsilon + 2\varepsilon_w} = \frac{f\,(\varepsilon_{\mathrm{Si}} - \varepsilon_w)}{\varepsilon_{\mathrm{Si}} + 2\varepsilon_w}.$$

The solution to the formula involves two complex roots. Enforcing the solution to be symmetric for water as a host and Si as an embedded grain in the composite and vice versa, the solution to Bruggeman's formula is

$$\varepsilon = \frac{b + \sqrt{8\varepsilon_w\varepsilon_{\mathrm{Si}} + b^2}}{4}; b = (f - 1)\varepsilon_{\mathrm{Si}} + (2 - 3f)\varepsilon_w.$$

The complex refractive index is given by $n + i\kappa = \sqrt{\varepsilon}$ and the penetration depth in the composite is calculated using $l = \lambda_0/4\pi\kappa$ for a free-space wavelength $\lambda_0 = c/f$; $c = 3 \times 10^8$ m/s and $f = 1$ GHz or 10 GHz.

Results for low-volume fraction of Si in water at 10 and 1 GHz are included in the main text.

[1] S. Sadat, A. Tan, Y. J. Chua, and P. Reddy, Nanoscale thermometry using point contact thermocouples, Nano Lett. **10**, 2613 (2010).

[2] G. Kucsko, P. C. Maurer, N. Y. Yao, M. Kubo, H. J. Noh, P. K. Lo, H. Park, and M. D. Lukin, Nanometer-scale thermometry in a living cell, Nature **500**, 54 (2013).

[3] V. Rieke and K. B. Pauly, MR thermometry, J. Magn. Reson. Imaging **27**, 376 (2008).

[4] D. Chalise, P. Kenesei, S. D. Shastri, and D. G. Cahill, Temperature mapping of stacked silicon dies using x-ray diffraction intensities, Phys. Rev. Appl. **18**, 1 (2022).

[5] H. A. Lorentz, *The Theory of Electrons and Its Applications to the Phenomena of Light and Radiant Heat* (G.E. Stechert, New York, B.G. Teubner, Leipzig, 1916).

[6] E. Seeram, *Computed Tomography: Physical Principles, Clinical Applications, and Quality Control*, 4th ed. (Elsevier Inc., St. Louis, Missouri, 2016).

[7] J. A. Grant, M. J. Morgan, J. R. Davis, and P. Wells, reconstruction strategy suited to x-ray diffraction tomography, J. Opt. Soc. Am. A **12**, 291 (1995).

[8] J. Chen, B. L. Daniel, and K. B. Pauly, Investigation of proton density for measuring tissue temperature, J. Magn. Reson. Imaging **23**, 430 (2006).

[9] P. A. Bottomley, T. H. Foster, R. E. Argersinger, and L. M. Pfeifer, A review of normal tissue hydrogen nmr relaxation times and relaxation mechanisms from 1–100 MHz: Dependence on tissue type, NMR frequency, temperature, species, excision, and age, Med. Phys. **11**, 98 (1984).

[10] K. J. Harry, *Non-Invasive Thermometry with Magnetic Resonance Imaging, in Theory and Applications of Heat Transfer in Humans 2V*, edited by D. Shrivastava (Wiley, Hoboken, New Jersey, 2018), 1st ed., p. 267.

[11] H. Odéen and D. L. Parker, Non-invasive thermometry with magnetic resonance imaging, Theory Appl. Heat Transfer Humans, 267 (2018).

[12] P. Wang, Evaluation of MR thermometry with proton resonance frequency method at 7 T, Quant. Imaging Med. Surg. **7**, 259 (2017).

[13] F. Bertsch, J. Mattner, M. Stehling, U. Müller-Lisse, M. Peller, R. Loeffler, J. Weber, K. Meßmer, W. Wilmanns, R. Issels, and M. Reiser, Non-invasive temperature mapping using MRI: Comparison of two methods based on chemical shift and T1-relaxation, Magn. Reson. Imaging **16**, 393 (1998).

[14] D. Bihan, J. Delaanoy, and R. Levin, Temperature mapping with MR imaging of molecular diffusion: application to hyperthermia, Ther. Radiol. **171**, 853 (1989).

[15] D. Chalise and D. G. Cahill, Highly sensitive and high throughput magnetic resonance thermometry of fluids using superparamagnetic nanoparticles, Phys. Rev. Appl. **19**, 1 (2023).

[16] L. J. Berliner and H. Fujii, Magnetic resonance imaging of biological specimens by electron paramagnetic resonance of nitroxide spin labels, Science **227**, 517 (1985).

[17] M. Azarkh and E. J. J. Groenen, Temperature determination by EPR at 275 GHz and the detection of temperature jumps in aqueous samples, J. Phys. Chem. B **119**, 13416 (2015).

[18] A. M. Portis, A. F. Kip, C. Kittel, and W. H. Brattain, Electron spin resonance in a silicon semiconductor, Phys. Rev. **90**, 988 (1953).

[19] G. Lancaster, J. A. Van Wyk, and E. E. Schneider, Spin-lattice relaxation of conduction electrons in silicon, Proc. Phys. Soc. **84**, 19 (1964).

[20] D. J. Lépine, Spin resonance of localized and delocalized electrons in phosphorus-doped silicon between 20 and 30 K, Phys. Rev. B **2**, 2429 (1970).

[21] R. J. Elliott, Theory of the effect of spin-orbit coupling on magnetic resonance in some semiconductors, Phys. Rev. **96**, 266 (1954).

[22] Y. Yafet, G factors and spin-lattice relaxation of conduction electrons, Solid State Phys. **14**, 1 (1963).

[23] J. L. Cheng, M. W. Wu, and J. Fabian, Theory of the spin relaxation of conduction electrons in silicon, Phys. Rev. Lett. **104**, 1 (2010).

[24] O. D. Restrepo and W. Windl, Full first-principles theory of spin relaxation in group-IV materials, Phys. Rev. Lett. **109**, 1 (2012).

[25] J. Park, J. J. Zhou, and M. Bernardi, Spin-phonon relaxation times in centrosymmetric materials from first principles, Phys. Rev. B **101**, 45202 (2020).

[26] W. Kohn, Shallow impurity states in silicon and germanium, Solid State Phys. **5**, 257 (1957).

[27] G. Feher, J. C. Hensel, and E. A. Gere, Paramagnetic resonance absorption from acceptors in silicon, Phys. Rev. Lett. **5**, 309 (1960).

[28] J. H. Pifer, Microwave conductivity and conduction-electron spin-resonance linewidth of heavily doped Si: P and Si: As, Phys. Rev. B **12**, 4391 (1975).

[29] Y. Song and H. Dery, Analysis of phonon-induced spin relaxation processes in silicon, Phys. Rev. B **86**, 1 (2012).

[30] Y. Song, O. Chalaev, and H. Dery, Donor-driven spin relaxation in multivalley semiconductors, Phys. Rev. Lett. **113**, 1 (2014).

[31] W. M. Bullis, *The Relationship Between Resistivity and Dopant Density for Phosphorus- and Boron-Doped Silicon*, (*National Bureau of Standards,* Washington, DC, 1973).

[32] G. Masetti, M. Severi, and S. Solmi, Modeling of carrier mobility against carrier concentration in arsenic-, phosphorus-, and boron-doped silicon, IEEE Trans. Electron Devices **30**, 764 (1983).

[33] H. Fritzsche, Resistivity and Hall coefficient of antimony doped germanium at low temperatures, J. Phys. Chem. Solids **6**, 69 (1958).

[34] G. Feher and A. F. Kip, Electron spin resonance absorption in metals. I. Experimental, Phys. Rev. **98**, 337 (1955).

[35] F. J. Dyson, Electron spin resonance absorption in metals. II. Theory of electron diffusion and the skin effect, Phys. Rev. **98**, 349 (1955).

[36] A. Niemöller, P. Jakes, R. A. Eichel, and J. Granwehr, EPR imaging of metallic lithium and its application to dendrite localisation in battery separators, Sci. Rep. **8**, 1 (2018).

[37] M. H. Brodsky and R. S. Title, Electron spin resonance in amorphous silicon, germanium, and silicon carbide, Phys. Rev. Lett. **23**, 581 (1969).

[38] G. K. Walters and T. L. Estle, Paramagnetic resonance of defects introduced near the surface of solids by mechanical damage, J. Appl. Phys. **32**, 1854 (1961).

[39] S. Qin and A. McTeer, Deep-depletion breakdown of Johnsen-Rahbek type electrostatic chuck operation for semiconductor processes, J. Appl. Phys. **104**, 1 (2008).

[40] C. Young, E. Poindexter, and G. Gerardi, Electron paramagnetic resonance of conduction-band electrons in silicon, Phys. Rev. B **55**, 16245 (1997).

[41] J. N. Chazalviel, Spin relaxation of conduction electrons in highly-doped n-type germanium at low temperature, J. Phys. Chem. Solids **36**, 387 (1975).

[42] M. Onda and K. Morigaki, ESR line width of as-doped germanium in the high concentration region, J. Phys. Soc. Japan **34**, 1107 (1973).

[43] E. B. Hale, J. R. Dennis, and S. H. Pan, Strain effects on the ESR spectrum from antimony donors in germanium, Phys. Rev. B **12**, 2553 (1975).

[44] P. Jiang, X. Qian, and R. Yang, Time-domain thermoreflectance (TDTR) measurements of anisotropic thermal conductivity using a variable spot size approach, Rev. Sci. Instrum. **88**, 1 (2017).

[45] A. Roy, M. Turner, and M. P. Sarachik, Susceptibility of Si: P across the metal-insulator transition. I. diamagnetism, Phys. Rev. B **37**, 5522 (n.d.).

[46] K. D. Cummings, J. C. Garland, and D. B. Tanner, Optical properties of a small-particle composite, Phys. Rev. B **30**, 4170 (1984).

[47] J. B. Hasted, *Aqueous Dielectrics*, 1st ed. (Chapman and Hall, London, 1973).

[48] K. Nortemann, J. Hillard, and U. Kaatze, Dielectric properties of aqueous NaCl at microwave frequencies, J. Phys. Chem. A **101**, 6864 (1997).

[49] A. Andryieuski, S. M. Kuznetsova, S. V. Zhukovsky, Y. S. Kivshar, and A. V. Lavrinenko, Water: Promising opportunities for tunable all-dielectric electromagnetic metamaterials, Sci. Rep. **5**, 1 (2015).

[50] R. T. Kinasewitz and B. Senitzky, Investigation of the complex permittivity of, J. Appl. Phys. **54**, 3394 (1983).

[51] M. van Exter and D. Grischkowsky, Optical and electronic properties of doped silicon from 0.1 to 2 THz, Appl. Phys. Lett. **56**, 1694 (1990).

[52] J. W. Cleary, R. E. Peale, D. J. Shelton, G. D. Boreman, C. W. Smith, M. Ishigami, R. Soref, A. Drehman, and W. R. Buchwald, IR permittivities for silicides and doped silicon, J. Opt. Soc. Am. B **27**, 730 (2010).

[53] A. Slaoui and P. Siffert, And relaxation time in heavily doped silicon, Phys. State Solid **89**, 617 (1985).

[54] S. S. Li and W. R. Thurder, The dopant density and temperature dependence of electron mobility and resistivity in N-type silicon, Solid State Electron. **20**, 609 (1977).

[55] H. M. Van Driel, Optical effective mass of high density carriers in silicon, Appl. Phys. Lett. **44**, 617 (1984).

[56] V. A. Markel, Introduction to the Maxwell Garnett approximation: Tutorial, J. Opt. Soc. Am. A **33**, 1244 (2016).